Highlights

Adaptive open-loop control for converter-based impedance spectroscopy in PV panels

Xin Wang, Zhixue Zheng, Michel Aillerie, Marie-Cécile Péra, Daniel Hissel

- Two key limitations in converter-based impedance spectroscopy (IS) are identified.
- The influences of various parameters on the limitations are systematically analyzed.
- An adaptive open-loop control method is developed for accurate online IS measurement.
- The proposed method is experimentally validated under diverse operating conditions.

Adaptive open-loop control for converter-based impedance spectroscopy in PV panels

Xin Wang^a, Zhixue Zheng^a, Michel Aillerie^b, Marie-Cécile Péra^a, Daniel Hissel^{a,c}

^aUniversité Marie et Louis Pasteur, UTBM, CNRS, institut FEMTO-ST, FCLAB, Belfort, F-90000, France ^bUniversité de Lorraine and CentraleSupelec, LMOPS, Metz, F-57000, France ^cInstitut Universitaire de France (IUF), Paris, F-75005, France

Abstract

Impedance information can reflect the internal relaxation processes of a system and is widely used for health monitoring. Converter-based impedance spectroscopy (IS) provides a promising approach for online applications by eliminating the need for additional equipment. However, its implementation encounters two key challenges: (1) resonance within the converter, caused by perturbation signal frequencies overlapping with the resonant frequency; and (2) limitations on the maximum perturbation frequency due to the converter bandwidth. These issues are particularly critical for photovoltaic (PV) panels, which require high perturbation frequencies ($\geq 1 \text{ kHz}$), leading to nonlinear perturbation signal injection and a reduction in IS measurement accuracy. To address these challenges, this paper systematically analyzes the factors contributing to these limitations using a conventional boost converter as a model. Based on the analysis, a basic design guide for setting converter's electrical components is provided. Meanwhile, the variation of perturbation signal amplitude with frequency is studied, and an adaptive open-loop control method is proposed. This method directly superimposes an adaptive ac duty cycle onto the control signal, ensuring sufficient and stable wideband signal injection. For experimental validation, the proposed method is compared with the traditional open-loop and two closed-loop control methods, providing their respective advantages and limitations. Furthermore, IS measurements under various irradiance levels and partial shading conditions are conducted, demonstrating the effectiveness of the proposed control method.

Keywords:

Adaptive open-loop control, frequency limitation, impedance spectroscopy, photovoltaic panel, resonance

1. Introduction

With the continued expansion of global economic activities and population growth, energy demand is increasing rapidly. Traditional fossil fuels such as coal and natural gas, which have long been central to industrial development, are now confronted with resource depletion and rising extraction costs [1]. In addition, the environmental impact of greenhouse gas emissions has further highlighted the importance of transitioning to renewable energy sources. Emission-free power generators and energy storage devices—such as fuel cells [2], photovoltaic (PV) panels, batteries, and supercapacitors—play a vital role in the power grid for industrial production, daily life [3], and transportation [4, 5]. Among these, PV panels are particularly favored due to their advantages, such zero noise, low pollution, no geographical limitations and ease of installation, etc. [6]. In addition to operating efficiency, the reliability of PV panels has become a critical factor in practical applications, which attracts growing attentions in recent years.

Impedance spectroscopy (IS) is an effective online tool to characterize the system's internal impedance across a wide frequency range. It is widely applied in fuel cells, batteries, and other electrochemical systems to monitor the system states or diagnose faults [7, 8, 9, 10]. Compared with the commonly used IV curve method for online health monitoring, IS measurement requires the PV panel to operate at a steady-state operating point, ensuring continuous output power during its implementation [11].

Traditional IS measurements rely on specialized frequency analyzers or workstations [12, 13]. Due to its relatively high cost, considerable volume and the constrained compatible voltage and current levels, it is more preferred for laboratory and cell-level applications. This has led to growing interest in online methods for IS implementation. In [14,

10], an excitation device for IS measurement system was designed to generate perturbation signals online. While these methods allow for online signal injection, they require additional circuitry, which not only increases cost but also adds complexity to the whole system. An alternative approach was presented in [15], where the impedance information was derived by analyzing the current oscillations of the switch. This method reduces costs and eliminates the need for injecting additional perturbation signals into the system, thereby minimizing the impact of IS measurements on system performance. However, at high frequencies, the amplitude of the oscillation current attenuates rapidly, which can significantly affect the accuracy of the measurements.

Converter-based IS enables the perturbation signal injection using the existing power converters [16, 17]. Due to the absence of additional hardware requirements and its lower cost, this approach has gained significant research interest. Authors in [18] proposed a novel multi-sinusoidal pulse-width modulation excitation method to inject perturbations online during regular battery operation, demonstrating strong consistency with the IS curves obtained from a commercial electrochemical workstation. A novel IS measurement technique based on full-bridge converter was investigated in [19], showing a good adaptability and accuracy. The converter-based IS measurement has also been applied to other converters [20, 21, 22, 14, 23], such as buck, boost, and dual-active-bridge converters, to analyze system health states, demonstrating its practicality in obtaining IS information of fuel cells and batteries online. However, this method remains primarily applied to fuel cells and batteries, with rare application to PV panels.

A cooperative control integrating maximum power point tracking (MPPT) and IS measurement based on a converter was proposed in [11]. Additionally, closed-loop control methods based on three commonly used compensation controllers were designed and compared. In [24], an adaptive Pseudo-Random Binary Sequence excitation method was introduced to obtain the impedance information of PV panels. Both studies verify the feasibility of implementing converter-based IS in PV panels to obtain internal impedance information. Authors in [25] established an equivalent circuit model of a PV panel and extracted the corresponding health features based on impedance information, validating the efficiency of converter-based IS in health monitoring of PV panels. Existing closed-loop control methods demonstrate the feasibility and effectiveness of health monitoring. However, these discussions are limited to the control strategies themselves and do not address the inherent limitations of converter-based IS. Moreover, they do not offer a fundamental-level analysis or a principled explanation of converter-based IS implementations. This highlights a critical research gap in understanding the underlying mechanisms of converter-based IS systems.

Due to the series connection of the inductor and the capacitor during switching (depending on the converter type), resonance may occur if the perturbation signal frequency range covers the resonant frequency [26]. This resonance increases the risk of the operating point entering the nonlinear region. It comprises the validity of IS measurement and lead to inaccurate measurement [27]. Additionally, the maximum frequency of the perturbation signal is constrained by the converter's bandwidth and operating conditions. A resonant controller was designed in [23] to alleviate the frequency limitation imposed by the traditional PI controller in the closed-loop control system. However, the issues of resonance and bandwidth limitations remain insufficiently addressed.

Therefore, this work focuses on addressing two key challenges in the implementation of converter-based IS. Using a conventional boost converter connected to a PV panel as a case study, the factors influencing resonance and the limitations on the maximum perturbation signal frequency are investigated. The effects of various parameters on the resonant peak and bandwidth are analyzed, providing a basic design guide for converters used for IS implementation.

Based on the analysis, a novel open-loop control method with an adaptive amplitude ac duty cycle is proposed. Unlike traditional open-loop control, this approach effectively mitigates resonance effects and improves measurement accuracy. Compared to closed-loop control, it eliminates the need for a controller, simplifying the design, enabling direct perturbation signal injection, and bypassing the constraints imposed by controller bandwidth. In summary, the key contributions of this study include:

- Systematic analysis of two key imitations in converter-based IS implementation: The state-space average
 model of a conventional boost converter considering all parasitic parameters, is derived to analyze the factors
 influencing resonance and the maximum perturbation signal frequency. These insights are crucial for designing
 converters and determining the perturbation frequency range for effective IS implementation.
- 2. Original design of an adaptive open-loop method for stable perturbation signal injection: To overcome limitations arising from resonance and converter bandwidth, a novel open-loop control method with an adaptive ac duty cycle is specifically designed to ensure reliable and accurate IS measurements.

3. Experimental implementation and validation under various operating conditions: A comprehensive comparison between the adaptive open-loop method and a closed-loop method is conducted. Meanwhile, experiments under different irradiance levels and partial shading percentages are performed to validate the effectiveness of the proposed control method.

This paper is organized as follows: Section II provides the fundamentals of converter-based IS. Section III analyzes the limitations of converter-based IS, including resonance and the maximum perturbation signal frequency, based on the state-space average model of a conventional boost converter. In Section IV, the setting principles for the converter's electrical components are given, and an adaptive open-loop control method is proposed to ensure stable online perturbation signal injection. Section V provides experimental validation of the proposed method under various operating conditions, and Section VI concludes this study.

2. Fundamentals of converter-based IS

The conventional boost converter, as the simplest type of step-up converter, is widely used in PV applications. Its topology, taking parasitic parameters into account, is illustrated in Fig. 1. Considering that the output current of the PV panel is influenced by its output voltage, a capacitor (C_1) is placed in parallel with the PV panel to stabilize the output voltage and maintain power delivery throughout each switching cycle under the discrete control [28]. In this study, C_1 is referred to as the support capacitor. The meaning of each parameter in Fig. 1 is summarized as follows:

S- PV panel; r_{pv} - parasitic resistance of the connecting line and junction box from the PV panel to the voltage sampling port; C_1 and r_{C_1} - support capacitor and its corresponding parasitic resistance; L and L- filter inductor and its corresponding parasitic resistance; L and L- filter inductor and its corresponding parasitic resistance; L- and L- power switch and its equivalent resistance when switched on; L- constant voltage source and on-resistance modeling the diode; L- and L- dc-bus capacitor and its corresponding parasitic resistance; L- load; L- output voltage and current of the PV panel; L- current flowing through the inductor; L- and L- voltage across and current through the support capacitor L- L- output voltage and current of the boost converter; L- voltage across and current through the dc-bus capacitor.

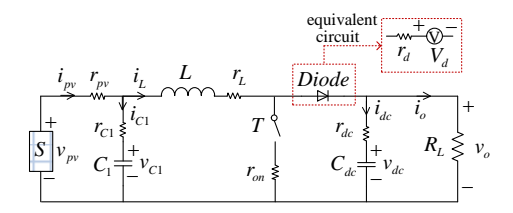


Figure 1: Topology of the conventional boost converter considering parasitic parameters.

The perturbation signal can be injected by controlling the duty cycle of the power switch T. According to the analysis in the previous study [11], the injection point should be located within the quasi-linear voltage region. As illustrated in Fig. 2, the IS spectrum is derived from the perturbation and response signals within a specific frequency range. For silicon PV panels, the frequency range of the perturbation signal can reach the kHz range. To ensure the validity of the IS measurement, four mathematical criteria, including linearity, causality, stability and finiteness, must be satisfied [29]. It necessitates keeping the amplitude of the perturbation signal small enough. Meanwhile, the amplitude must be sufficiently large to ensure a good signal-to-noise ratio (SNR) of the IS measurement.

However, resonance caused by the series connection of the inductor L and the dc-bus capacitor C_{dc} when the switch is off can lead to a peak in the amplitude of the perturbation signal, if the ac duty cycle amplitude is always kept constant. The resonance-induced peak may derive the PV panel into the nonlinear region [27]. Additionally, the converter's bandwidth limits the amplitude of the perturbation signal at high frequencies, thereby reducing its SNR. Both aspects can compromise the accuracy of the IS measurement. Therefore, to achieve a perturbation signal that is both effective and sufficient, it is essential to thoroughly analyze the factors influencing these two limitations.

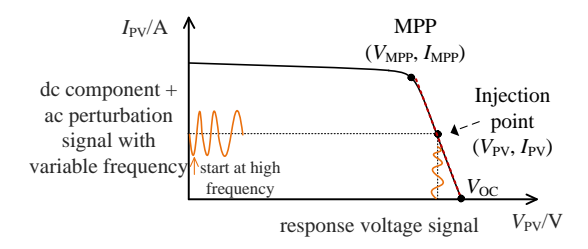


Figure 2: Injection point and perturbation signal for IS implementation.

3. Limitations of converter-based IS

3.1. State-space average model

The state-space average model is a widely used technique for deriving an average, linearized model of switching converters [30]. To analyze the resonance behavior of the conventional boost converter during the perturbation signal injection, the average model of the boost converter, as shown in Fig. 1 can be expressed as:

when the switch T is on:

$$\begin{cases}
L\frac{di_L(t)}{dt} = v_{pv}(t) - i_{pv}(t) \cdot r_{pv} \\
-i_L(t) \cdot r_L - i_L(t) \cdot r_{on}
\end{cases}$$

$$\begin{cases}
C_1 \frac{dv_{C_1}(t)}{dt} = i_{C_1}(t) \\
C_{dc} \frac{dv_{dc}(t)}{dt} = i_{dc}(t)
\end{cases}$$
(1)

when the switch T is off:

$$\begin{cases} L \frac{di_{L}(t)}{dt} = v_{pv}(t) - i_{pv}(t) \cdot r_{pv} - i_{L}(t) \cdot r_{L} \\ - i_{L}(t) \cdot r_{d} - V_{d} - v_{o}(t) \end{cases}$$

$$\begin{cases} C_{1} \frac{dv_{C_{1}}(t)}{dt} = i_{C_{1}}(t) \\ C_{dc} \frac{dv_{dc}(t)}{dt} = i_{dc}(t) \end{cases}$$
(2)

In order to derive the equations for all state variables, Kirchhoff's voltage law (KVL), Kirchhoff's current law (KCL) and Ohm's law are applied as follows:

$$\begin{cases} v_{pv}(t) = i_{pv}(t) \cdot r_{pv} + v_{C_1}(t) + i_{C_1}(t) \cdot r_{C_1} \\ i_{pv}(t) = i_L(t) + i_{C_1}(t) \\ v_o(t) = v_{dc}(t) + i_{dc}(t) \cdot r_{dc} \\ i_o(t) = \frac{v_o(t)}{R_L} \\ \begin{cases} i_{dc}(t) = -i_o(t) \\ i_{dc}(t) = -i_o(t) + i_L(t) \end{cases} \text{ (the power switch is on)} \end{cases}$$
(3)

To derive the linearized model of the conventional boost converter around a steady-state duty cycle, i.e., D, a direct small-signal perturbation, i.e., \hat{d} , is superimposed. All variables are equal to a sum of a dc component and a small-signal perturbation, i.e., $d = D + \hat{d}$, $v_{pv} = V_{pv} + \hat{v}_{pv}$, $v_o = V_o + \hat{v}_o$, $i_{pv} = I_{pv} + \hat{i}_{pv}$, $i_{C1} = I_{C1} + \hat{i}_{C1}$, $i_L = I_L + \hat{i}_L$, $i_o = I_o + \hat{i}_o$. Based on (1), (2), (3) and Laplace transform, the small-signal transfer function from the duty cycle to the

output current of the PV panel, i.e., $G_{i_{pv}-d}(s)$ can be derived:

$$G_{i_{pv}-d}(s) = \frac{\hat{i}_{pv}(s)}{\hat{d}(s)}|_{\hat{v}_{pv}=0}$$

$$= \frac{\hat{i}_{pv}(s)}{\hat{i}_{L}(s)} \cdot \frac{\hat{i}_{L}(s)}{\hat{d}(s)}|_{\hat{v}_{pv}=0} = G_{i_{pv}-i_{L}}(s) \cdot G_{i_{L}-d}(s)$$

$$= K_{i_{L}-d0} \cdot \frac{(1 + \frac{s}{\omega_{2-i_{pv}}})(1 + \frac{s}{\omega_{2-i_{L}}})}{(1 + \frac{s}{\omega_{0-i_{pv}}})(1 + \frac{1}{Q}\frac{s}{\omega_{0-i_{L}}} + (\frac{s}{\omega_{0-i_{L}}})^{2})}$$
(4)

where K_{i_L-d0} is the gain of the converter, when the frequency is going down to 0 Hz; $\omega_{z-i_{PV}}$ and $\omega_{0-i_{PV}}$, represent the frequency of the zero of the numerator and the natural frequency of the transfer function $G_{i_{PV}-i_L}(s)$, respectively; ω_{z-i_L} and ω_{0-i_L} represent the frequency of the zero of the numerator and the natural frequency of the transfer function $G_{i_L-d}(s)$, respectively; Q represents the quality factor. Their values can be expressed as:

$$\begin{cases} \omega_{z-i_{PV}} = 1/(C_{1}r_{C1}) \\ \omega_{0-i_{PV}} = 1/(C_{1}(r_{C1} + r_{pv})) \\ K_{i_{L}-d0} = \frac{2V_{o} - V_{par}}{(1 - D)^{2}R_{L} + r_{par}} \\ \omega_{z-i_{L}} = \frac{2V_{o} - V_{par}}{V_{o}C_{dc}(R_{L} + 2r_{dc}) - V_{par}C_{dc}(R_{L} + r_{dc})} \\ \omega_{0-i_{L}} = \sqrt{\frac{(1 - D)^{2}R_{L} + r_{par}}{LC_{dc}(R_{L} + r_{dc})}} \\ Q = \frac{\sqrt{(1 - D)^{2}R_{L} + r_{par} \cdot \sqrt{LC_{dc}(R_{L} + r_{dc})}}}{(1 - D)^{2}R_{L}C_{dc}r_{dc} + L + r_{par}C_{dc}(R_{L} + r_{dc})} \\ V_{par} = I_{L}(r_{on} - r_{d}) - V_{d} \\ r_{par} = r_{pv} + r_{L} + r_{d} + D(r_{on} - r_{d}) \end{cases}$$

$$(5)$$

where V_{par} and r_{par} , represent the average parasitic voltage and parasitic resistance over one switching cycle, respectively. It should be noted that during the calculation, the differential products, i.e., $\hat{d}(s)\hat{i}_L(s)$ and $\hat{d}(s)\hat{v}_o(s)$ are ignored herein.

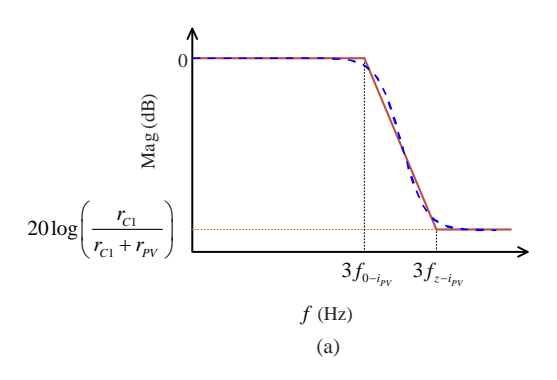
It can be observed in (4) that $G_{i_{pv}-d}(s)$ consists of two components: the first, denoted as $G_{i_{pv}-i_L}(s)$, and the second, referred to as $G_{i_L-d}(s)$. The corresponding asymptotic magnitude plots of these two components are illustrated in Fig. 3, where the dotted and solid lines represent the actual and asymptotic values, respectively. Additionally, the parameters $f_{0-i_{pv}} = \omega_{0-i_{pv}}/2\pi$, $f_{z-i_{pv}} = \omega_{z-i_{pv}}/2\pi$, $f_{z-i_L} = \omega_{z-i_L}/2\pi$ and $f_{0-i_L} = \omega_{0-i_L}/2\pi$ are defined.

Considering that $f_{0-i_{pv}} > f_{0-i_L}$, as calculated using the parameters provided in Table. 1 in Section IV. A, the variation in the perturbation signal's magnitude with respect to frequency can be segmented into three regions: (1) an approximately constant value from 0 to f_{z-i_L} , (2) an increasing value within the range $[f_{z-i_L}, f_{0-i_L}]$, and (3) a decreasing value with a slope of k_{slope} when the frequency exceeds f_{0-i_L} . Therefore, the factors influencing the two limitations of converter-based IS measurements can be analyzed across three key parameters: resonant frequency, magnitude at the resonant frequency, and maximum perturbation signal frequency, which will be further analyzed below.

3.2. Resonance information

As shown in Fig. 3, the peak caused by the series connection of the inductor L and dc-bus capacitor C_{dc} occurs at the resonant frequency, i.e., f_0 , and corresponding value can be expressed as:

$$f_0 \approx f_{0-i_L} = \frac{1}{2\pi} \cdot \sqrt{\frac{(1-D)^2 R_L + r_{par}}{L C_{dc}(R_L + r_{dc})}}$$
 (6)



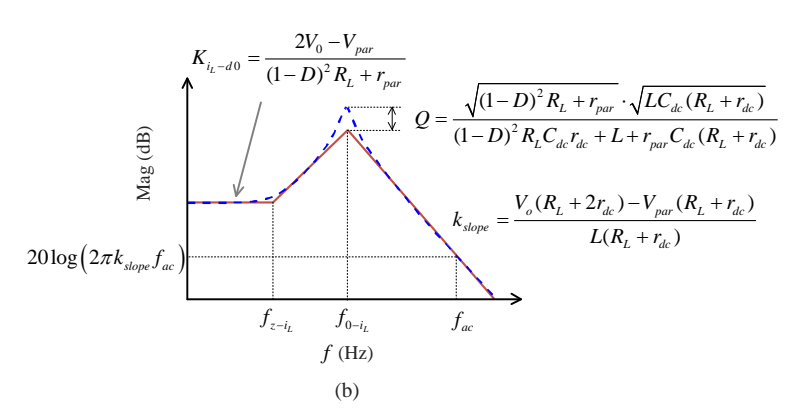


Figure 3: Asymptotic magnitude plots of (a) $G_{i_{pv}-i_L}(s)$ and (b) $G_{i_{L-d}}(s)$.

To minimize power losses, the parasitic parameters should be significantly smaller than the load, resulting in the simplification of (6) as follows:

$$f_0 \propto \frac{1}{2\pi} \cdot \frac{(1-D)}{\sqrt{LC_{dc}}} \tag{7}$$

It can be observed that the main factors influencing the resonant frequency are D, L and C_{dc} . Specifically, f_0 is inversely proportional to the square root of the product of L, C_{dc} and directly proportional to 1 - D. The parasitic parameters slightly affect the value of f_0 based on (6): f_0 increases when r_{PV} and r_L increase and when r_{dc} decreases. It is worth noting that the impacts of r_{PV} , r_L and r_{dc} on f_0 is closely tied to the value of R_L . A higher R_L reduces the relative variation in f_0 .

By substituting (6) into (4), the magnitude of $G_{i_1-d}(s)$ at f_0 can be determined as:

$$|G_{i_L-d-f_0}(s)| \approx \frac{V_o(R_L + 2r_{dc}) - V_{par}(R_L + r_{dc})}{L(R_L + r_{dc})\omega_0} + Q$$

$$= \frac{(V_o(R_L + 2r_{dc}) - V_{par}(R_L + r_{dc}))\sqrt{C_{dc}}}{\sqrt{L(R_L + r_{dc})((1 - D)^2R_L + r_{par})}}$$

$$+ \frac{\sqrt{(1 - D)^2R_L + r_{par}} \cdot \sqrt{LC_{dc}(R_L + r_{dc})}}{(1 - D)^2R_LC_{dc}r_{dc} + L + r_{par}C_{dc}(R_L + r_{dc})}$$
(8)

Considering the relative value between the parasitic and other parameters, i.e., $V_{par} \ll V_o$, r_{dc} and $r_{par} \ll R_L$, it can be concluded that the value of the peak at resonant frequency indicated in (8) is primarily determined by the electrical components, L and C_{dc} , as well as the operating parameters, V_o , D and R_L . By ignoring the parasitic parameters, the influence of electrical components and operating parameters on the resonant peak can be estimated, as shown below:

$$|G_{i_L - d - f_0}(s)| \propto \sqrt{\frac{C_{dc}}{L}} \left(\frac{V_o}{1 - D} + (1 - D)R_L \right)$$
 (9)

Additionally, (8) illustrates the equivalent parasitic parameters, i.e., $V_{par} = I_L(r_{on} - r_d) - V_d r_{par} = r_{pv} + r_L + r_d + D(r_{on} - r_d)$ and r_{dc} will affect the value of resonant peak. Disregarding the product terms of parasitic parameters, the individual influence of r_{dc} , V_{par} and r_{par} can be summarized as follows:

• r_{dc} : given that $r_{dc} \ll R_L$, the influence of the r_{dc} on the resonant peak can be estimated as follows:

$$|G_{i_L-d-f_0}(s)| \propto \frac{\sqrt{(1-D)^2R_L + r_{par}} \cdot \sqrt{LC_{dc}R_L}}{(1-D)^2R_LC_{dc}r_{dc} + L + r_{par}C_{dc}R_L}$$

It shows that an increase in r_{dc} leads to a decrease in the resonant peak.

• V_{par} : the influence of V_{par} can simplified as:

$$|G_{i_L-d-f_0}(s)| \propto \frac{-V_{par}(R_L+r_{dc})\sqrt{C_{dc}}}{\sqrt{L(R_L+r_{dc})((1-D)^2R_L+r_{par})}},$$

It indicates the value of the resonant peak is inversely proportional to the value of V_{par} .

• r_{par} : the influence of r_{par} on resonant peak depends on the relative value between $(1-D)^2R_L$ and r_{par} . Generally, the condition $r_{par} \ll (1-D)^2R_L$ holds, allowing (8) to be approximately expressed as:

$$|G_{i_L-d-f_0}(s)| \propto \frac{\sqrt{(1-D)^2 R_L} \cdot \sqrt{LC_{dc}(R_L + r_{dc})}}{(1-D)^2 R_L C_{dc} r_{dc} + L + r_{par} C_{dc}(R_L + r_{dc})},$$

It can be concluded that the resonant peak decreases as r_{par} increases.

Meanwhile, based on the magnitude function shown in (8) and the values listed in Table 1, a sensitivity analysis is carried out to examine how variations in key components and their parasitic parameters influence the resonance. And each parameter is varied within its tolerance range (using a commonly applied $\pm 5\%$ tolerance level), as indicated in Fig. 4. It is clear that the increasing the value of the parasitic parameters, except the constant voltage source of the diode V_d , can help reduce the impact of resonance. However, the power loss will also increase. Hence, the parasitic parameters cannot be too large due to the limitation of converter efficiency, which should generally be greater than 95%.

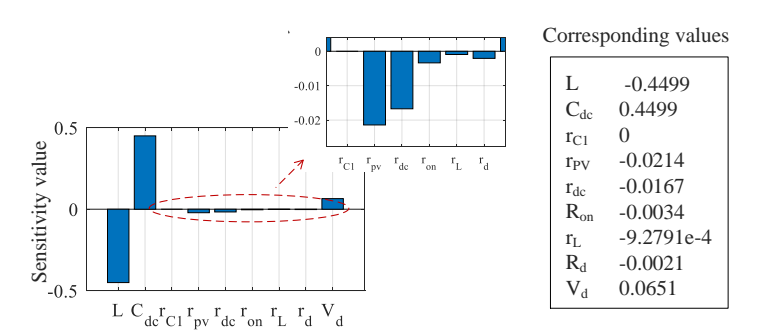


Figure 4: Sensitivity analysis of parameter variations on resonance.

3.3. Maximum perturbation signal frequency

Based on the asymptotic magnitude plots of $G_{i_{pv}-i_L}$ and G_{i_L-d} depicted in Fig. 3, the amplitude of the perturbation signal is influenced by both its frequency and the amplitude of the ac duty cycle. To ensure the validity of the IS measurement, a target amplitude for the perturbation signal will be defined based on the dc components of the output current of the PV panel, and can be expressed as:

$$I_{ac} = K_{per} I_{pv} \tag{10}$$

where K_{per} represents the percentage between I_{ac} and I_{pv} at the injection point.

The amplitude of the ac duty cycle is limited by the modulation. Without considering the over-modulation conditions, the maximum value of the ac duty cycle amplitude is given by:

$$d_{ac-max} = 0.5 - |0.5 - D| \tag{11}$$

According to the expressions in (10) and (11), the magnitude of $G_{i_{pv}-d}(s)$ at the maximum perturbation signal frequency, denoted as f_{max} , is given by $20\log(I_{ac}/d_{ac-max})$. Therefore, the value of f_{max} is assumed to be:

$$f_{max} = \frac{1}{2\pi} \cdot \frac{r_{C1}}{(r_{C1} + r_{PV})} \cdot \frac{V_o(R_L + 2r_{dc}) - V_{par}(R_L + r_{dc})}{L(R_L + r_{dc})} \cdot \frac{d_{ac-max}}{I_{ac}}$$
(12)

Substituting (10) and (11) to (12), the influence of all system parameters can be summarized as follows:

1. Influence of electrical components:

$$f_{max} \propto 1/L$$
 (13)

2. Influence of parasitic parameters:

$$f_{max} \propto \begin{cases} r_{C1} / \left(r_{C1} + r_{pv} \right) \\ r_{dc} / \left(R_L + r_{dc} \right) \\ -V_{par} \end{cases}$$
 (14)

3. Influence of operating parameters:

$$f_{max} \propto \frac{d_{ac-max}V_{pv}}{(1-D)K_{per}I_{pv}} \tag{15}$$

Equations (13), (14) and (15) demonstrate that an increase in r_{C1} and r_{dc} leads to an increase in f_{max} ; while an increase in L and r_{pv} results in a decrease. A detailed comparison of the influence of the components and their corresponding parasitic parameters on f_{max} is provided through a sensitivity analysis, as illustrated in Fig. 5. It should be noticed that an increase in K_{per} will reduce the maximum perturbation signal frequency. As for the influence of operating parameters, the coupling of these three parameters, i.e., D, V_{pv} and I_{pv} , should be considered.

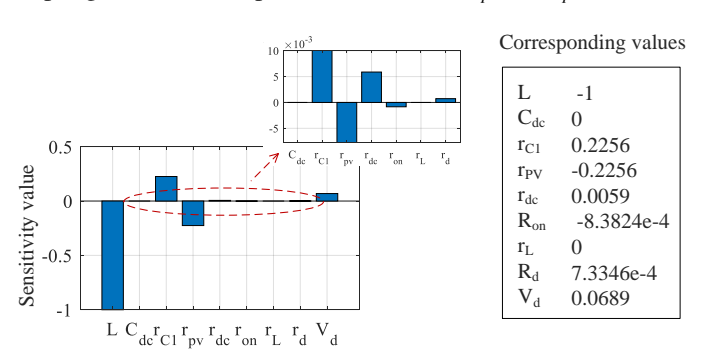


Figure 5: Sensitivity analysis of parameter variations on f_{max} .

4. Adaptive open-loop control method

As analyzed above, certain parameters affect the resonant frequency, resonant peak and maximum perturbation signal frequency. By adjusting the amplitude of the ac duty cycle, a stable perturbation signal can be maintained. Regulation methods typically involve two categories: closed-loop control (using controllers) and open-loop control (direct calculation). In closed-loop control, the maximum perturbation signal frequency achieved is lower than the value calculated by (12), due to controller bandwidth limitations [11]. In contrast, traditional open-loop control directly adds a constant-amplitude ac duty cycle to the dc duty cycle, but this can lead to inaccuracies caused by resonance and frequency limitations. This section discusses parameter setting principle and propose an adaptive open-loop control method based on the chosen parameters.

4.1. Setting principle of electrical components

4.1.1. Setting principle of the inductor L

The relationship between the current ripple Δi_L and the inductance in the conventional boost converter can be written as:

$$L = \frac{1}{\Delta i_L} \cdot (1 - D) \cdot T_{sw} \cdot (V_o - V_{pv}) \tag{16}$$

where T_{sw} represents the switching period and is set to $1/(8 \times 10^4)$ s, corresponding to a switching frequency of 80 kHz. After performing the linearity tests [31], and evaluating the signal-to-noise ratio (SNR), the amplitude of the perturbation signal was selected to be in the range of 15%–20% in our experiments. Thus, the percentage of the current ripple in our platform design is kept below 5%. And the inductor value is set to 2.5 mH, ensuring that the peak of the current ripple remains less than half of I_{ac} across the entire testing current range.

4.1.2. Setting principle of the support capacitor C_1

The output current of the PV panel is closely related to its output voltage [28]. To ensure a stable output voltage during each switching cycle, a hold-on capacitor C_1 is placed in parallel with the PV panel. When the switch is turned on, C_1 operates in discharging state, and the voltage across C_1 can be described as:

$$v_{C_1}(t) = \sqrt{K_1^2 + K_2^2} e^{-\alpha t} \cos(\omega_{d-C_1} t - \arctan\frac{K_2}{K_1})$$
(17)

where

$$\begin{cases} \alpha = (r_{C1} + r_L + r_{on})/(2L) \\ \omega_{d-C_1} = \sqrt{1/(LC_1) - \alpha^2} \\ K_1 = v_{C_1}(0) = V_{pv} \\ K_2 = \frac{1}{\omega_{d-C_1}} (\frac{i_L(0)}{C_1} + \alpha V_{pv}) \end{cases}$$

 $v_{C_1}(0)$ and $i_L(0)$ represent the initial value of v_{C_1} and i_L .

To ensure the output voltage remains stable across the entire duty cycle range (D from 0 to 1), always, the value of t is set to T_{sw} . Based on the requirement for the output voltage ripple of the PV panel during IS implementation (limited to $\leq 0.1 \ V$), the value of C_1 can be calculated: $C_1 \geq 114.6 \ uF$. Finally, three parallel capacitors, each with a capacitance of 47 uF and a total capacitance of 141 uF, are selected in the experimental platform.

4.1.3. Setting of the dc-bus capacitor C_{dc}

The value of the dc-bus capacitor C_{dc} is determined based on the dc-bus voltage ripple ΔV_o . Their relationship is satisfied as:

$$C_{dc} = DT_{sw}V_o/R_L\Delta V_o \tag{18}$$

The dc-bus voltage ripple is typically set below 5%. In experimental platform, a SiC power module (PEB 8024) with an integrated 260 uF dc-bus capacitor is selected. It can maintain the dc-bus voltage ripple within the acceptable range, thus no modification is made to the dc-bus capacitor.

Considering the commercially available components, the converter efficiency and the maximum achievable f_{max} , all parameters used in the platform are summarized in Table. 1. Based on these parameters, the magnitude of $G_{i_{pv}-d}(s)$ is plotted in MATLAB, as shown in Fig. 6. The magnitude starts to increase at $f_{z-i_L} = 7.27$ Hz, with the resonant frequency at 108.82 Hz, and the theoretical maximum perturbation signal frequency reaching 12.2 kHz.

4.2. Adaptive open-loop control method

To ensure a stable perturbation signal, the amplitude of superimposed ac duty cycle should vary with frequency. As indicated in Fig. 3, the magnitude of $G_{i_{PV}-d}(s)$ change trend transitions at the frequencies change trend changes at frequency f_{z-i_L} and f_{0-i_L} . Taking into account the maximum perturbation frequency, the change in the magnitude of $G_{i_{PV}-d}(s)$ with frequency can be segmented into three distinct frequency ranges:

• [0 f_{z-i_L}]: the magnitude of $G_{i_{PV}-d}(s)$ can be seen as a constant value and is approximately equal to $20log(K_{i_L-d0})$

.

Table 1: Setting of system parameters in this study

Parameters	Value	Parameters	Value
V_{pv}	34 V	r_{pv}	0.3 Ω
I_{pv}	0.7 A	r_L	0.013 Ω
D	0.45	r_{C1}	1.03 Ω
C_1	3*47 uF	r_{on}	0.08Ω
L	2.5 mH	r_d	0.07 Ω
R_L	160 Ω	V_d	4.6 V
C_{dc}	260 uF	r_{dc}	1.03 Ω

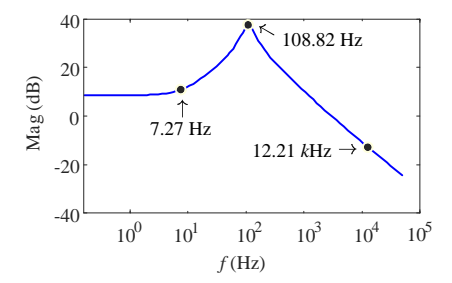


Figure 6: Magnitude plot of $G_{i_{pv}-d}(s)$ with the set parameters.

- $(f_{z-i_L} f_0]$: the magnitude of $G_{i_{PV}-d}$ approximately increases with frequency, following a ramp function with a slope of $2\pi k$, where $k = (2\pi k_{slope} f_0 K_{i_L-d0})/2\pi (f_0 f_{z-i_L})$.
- $(f_0 f_{max}]$: the magnitude of $G_{i_L-d}(s)$ decreases with a slope of k_{slope} , while the magnitude of $G_{i_{PV}-i_L}(s)$ is determined by the ratio $(r_{C1} + r_{PV})/r_{C1}$.

Thus, the corresponding magnitudes and adaptive values of the ac duty cycle amplitude across different frequency ranges can be calculated from the above analysis of the variation in the magnitude of $G_{i_{PV}-d}(s)$, along with the amplitude of the perturbation signal given in (10), with the results provided in Table. 2, where f_{ac} represents the perturbation signal frequency.

Table 2: Adaptive amplitude for perturbation signal

Frequency	Magnitude	Adaptive amplitude
f_{ac}	$G_{i_{PV}-d}(s)$	d_{ac}
$[0 f_{z-i_L}]$	K_{i_L-d0}	$K_{per}I_{pv}/K_{i_L-d0}$
$(f_{z-i_L} f_0]$	$K_{i_L-d0}+$	$K_{per}I_{pv}$
	$2\pi k(f_{ac}-f_{z-i_L})$	$\frac{K_{i_L-d0} + 2\pi k (f_{ac} - f_{z-i_L})}{K_{per} I_{pv} \cdot (r_{C1} + r_{PV})}$
$(f_0 f_{max}]$	$2\pi r_{C1}k_{slope}f_{ac}$	$K_{per}I_{pv}\cdot(r_{C1}+r_{PV})$
	$r_{C1} + r_{pv}$	$2\pi r_{C1}k_{slope}f_{ac}$

According to the selected parameters and the summary in Table, the corresponding amplitudes of the perturbation signal are illustrated as the blue line in Fig. 7. Compared with the perturbation signal generated based on a constant ac duty cycle, represented by the black line in Fig. 7, the adaptive open-loop control can effectively reduce the influence of resonance, resulting in a more stable perturbation signal (ranging from $0.15 I_{pv}$ to $0.20 I_{pv}$).

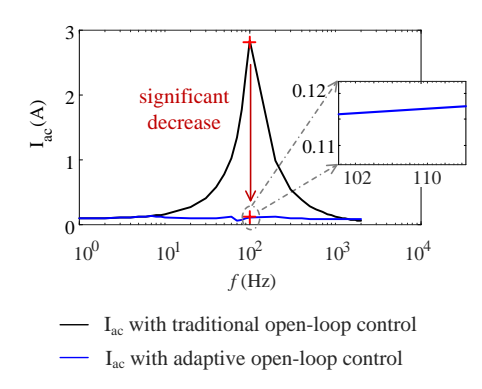


Figure 7: Perturbation signal amplitudes under the traditional and adaptive open-loop control.

5. Experimental validation

An experimental platform has been developed in the laboratory for online IS implementation and verification, as shown in Fig. 8. A dSPACE SCALEXIO box is used as the digital controller to generating and collect the perturbation signal and its corresponding responses. Current measurement is conducted using a high-accuracy current transducer (IT 65-S ULTRSTAB) with a wide frequency bandwidth. Power conversion is achieved with a half-bridge SiC power module (PEB 8024) with an integrated dc bus capacitor (260 μ F). For the online tests, the switching frequency is set as 80 μ Hz. A monocrystalline PV module (RECOM-Sillia 60M310) is integrated into our platform, with a short-circuit current of 9.95 A and an open-circuit voltage of 39.6 V. Additional parameters are provided in the Appendix. Considering the characteristics of the PV panel and the influence of parasitic parameters, the perturbation signal frequency range is set as [1 Hz 2 μ Hz].



Figure 8: Experimental platform for online IS implementation and verification.

5.1. Verification of adaptive open-loop control method

In traditional open-loop control, the ac duty cycle with constant amplitude is superimposed on a fix dc duty cycle to achieve online perturbation at the injection point, as shown in Fig. 9 (a). The experimental waveforms of the output current and voltage of the PV panel are shown in Fig. 10 (a). A significant peak is observed in the output current signal during IS implementation. By analyzing the measurements, the amplitude of the corresponding perturbation signal is obtained, as shown in the lower left corner of Fig. 10 (a). The peak occurs within the frequency range of 100 Hz to 110 Hz, which aligns with the system's resonant frequency. As a consequence of resonance, the operating point deviates from the linear operating region. Moreover, as the frequency increases, the amplitude of the perturbation

signal decreases, making it increasingly difficult to obtain accurate voltage and current information, even though the frequency remains below the theoretical maximum perturbation signal frequency.

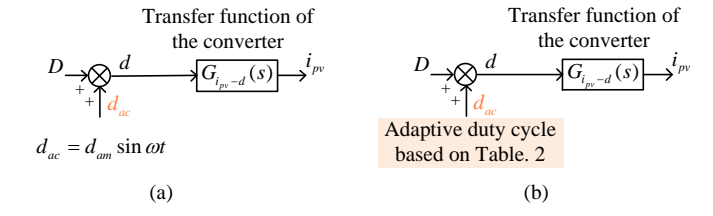
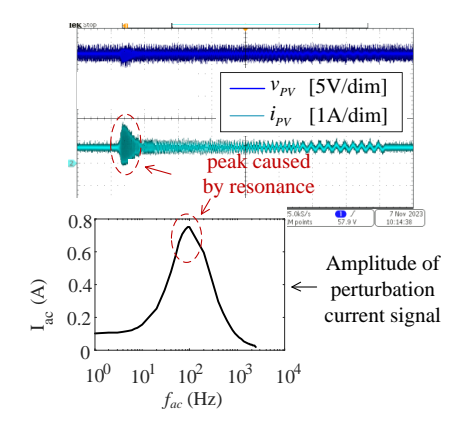
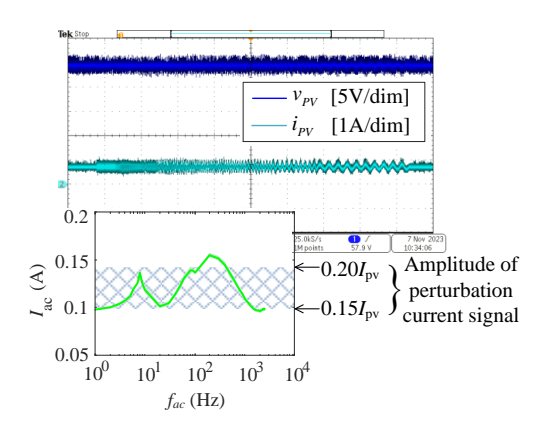


Figure 9: Control blocks of the traditional and adaptive open-loop control methods: (a) traditional open-loop control; (b) adaptive open-loop control.





- (a) Experimental waveforms in traditional open-loop control.
- (b) Experimental waveforms in adaptive open-loop control.

Figure 10: Comparison of the experimental waveform in traditional open-loop control and adaptive open-loop control.

Meanwhile, the adaptive open-loop control indicated in Fig. 9 (b) is implemented to achieve online perturbation, and the corresponding experimental waveforms are shown in Fig. 10 (b). It can be observed that the peak caused by resonance is significantly reduced, as illustrated by the green line. Most of the green line falls with the shadowed area (from $0.15I_{pv}$ to $0.20I_{pv}$, a range that ensures both accurate signal sampling and valid IS measurement). This indicates the successful maintenance of a stable perturbation signal over the entire frequency range.

For the IS measurements, at least ten repetitions were performed under each operating condition. The PV panel's Impedance characteristics were derived from the perturbation and response signals, and the averaged magnitude and phase values in the Bode plot were calculated within a 95% confidence interval, as shown in Fig. 11 (a), which corresponds to measurements obtained using the adaptive open-loop method at an irradiance of $284 \ W/cm^2$ and a current operating point 0.7 A. The corresponding IS curve in the Nyquist representation was then calculated from these averaged values, as illustrated in Fig. 11 (b). Using the same methodology, the impedance spectra for different control strategies and different irradiance levels, represented as groups of Nyquist curves, are directly shown in Fig. 12 and Fig. 13, respectively.

As discussed in [11], the closed-loop control method can also achieve stable perturbation signal injection. A comparison between the open-loop and closed-loop control methods is thus conducted. The corresponding impedance spectra, represented as a group of Nyquist curves, are shown in Fig. 12.

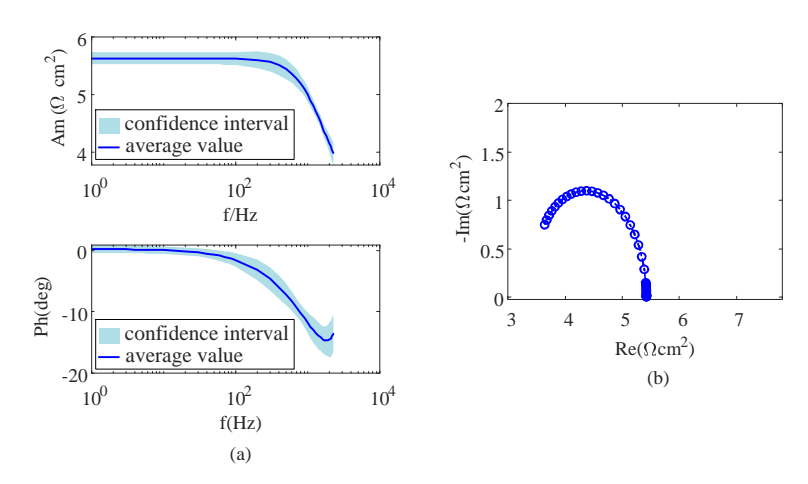


Figure 11: Impedance curves (a) IS curve in the Bode representation with a 95% confidence interval (b) IS curve in the Nyquist representation with average values.

14

Table 3: Comparison of open-loop and closed-loop control strategies.

Control methods		Open-loop control		Close-loop control	
		Traditional open-loop control	Adaptive open-loop control	Unified control [11]	Hybrid control [11]
Control complexity -	Perturbation type	Superimpose constant	Superimpose adaptive	Rely on specific design	Rely on specific design
		ac duty cycle	ac duty cycle	of the single controller	of the hybrid controller
	Execution time	0.0027 s		0.0034 s	0.0041 s
Injection point	Location accuracy	98.57%	98.57%	99.5%	99.2%
Injection point	Stability	Significantly influenced by operating conditions		Automatically adjustable to variable operating condition	
Perturbation signal	Amplitude accuracy	Exceed the target amplitude cause an abnormal area (area 1 in Fig. 12)	88.47%	93.7%	96.5%
	SNR	Very poor SNR at high frequency cause an abnormal area (area 2 in Fig. 12)	9.4 dB	6.9 dB	5.2 dB
	Frequency constraint	Limited by the characteristics of the converter		Limited by the characteristics of both the converter and controller (< 1/9 closed-loop crossover frequency)	
	Time delay	Smaller delay influence the accuracy		Generally larger delay, affect the stability and accuracy	
Practical issues in control	Sampling noise	No feedback, minimal effect		Feed back into the control loop, requires filtering	
	Saturation effect	Output clipped at saturation, and accuracy degraded		Integrator windup at saturation; potential instability (overshoot, oscillations, etc.)	

Unified control: a unified PI controller
Hybrid control: P controller + quasi-proportional resonant (QPR) controller
Execution time: the time required for a single execution of the perturbation signal injection method, without considering the effects of filtering or other factors
Version of PC: Dell InC. Intel(R) Core(TM) i5-10210U CPU 1.60GHz 2.11 GHz

Version Matlab: 2020 b

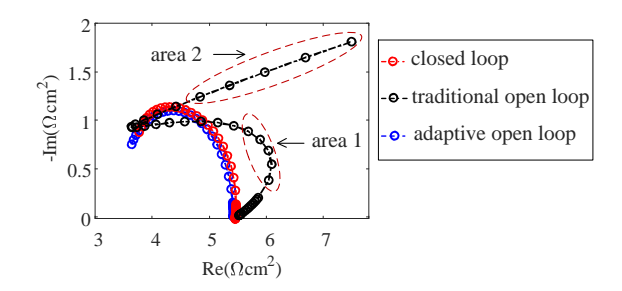


Figure 12: Comparison of IS measurements under different control methods.

Fig. 12 shows that under traditional open-loop control with a constant ac duty cycle amplitude, two abnormal regions, labelled as "area 1" and "area 2", can affect the description accuracy of the PV panel performance characterization based on IS measurements. "Area 1" arises from resonance, with deviations from expected impedance values, quantified by the Euclidean distance ranging from 5.04% to 12.38%. "Area 2" is caused by reduced accuracy in the sampled data when the amplitudes of the perturbation current and response voltage signals are small, leading to apparent high-frequency capacitive divergence that contradicts the PV panel's underlying physical processes [25]. In contrast, when using either the closed-loop control or the proposed adaptive open-loop control method, the quality of the perturbation signals improves, resulting in Nyquist curves with high precision. Moreover, the impedance spectra obtained from both methods exhibit good consistency across the overall frequency range.

A detailed comparison between the proposed adaptive open-loop, traditional open-loop and two closed-loop control methods is summarized in Table. 3. Compared to the closed-loop control, the proposed open-loop control offers several advantages: it eliminates the needs for controller design and is not limited by controller bandwidth. Moreover, it achieves a favorable SNR of 9.4 dB for the perturbation signal, which indicates that the perturbation signal power is around nice times higher than the noise power. However, it exhibits slightly lower accuracy in locating the injection point, which is reasonable given the absence of closed-loop control.

5.2. Verification under different irradiance levels

Irradiance is one of the crucial factors influencing the performance of PV panels. IS measurements under six different irradiance levels have been obtained using the adaptive open-loop control method, at the injection point of $I_{pv} = 0.7 \text{ A}$: $G_1 = 218 \text{ W/m}^2$, $G_2 = 226 \text{ W/m}^2$, $G_3 = 250 \text{ W/m}^2$, $G_4 = 263 \text{ W/m}^2$, $G_5 = 268 \text{ W/m}^2$, $G_6 = 284 \text{ W/m}^2$. The corresponding IS spectra is depicted in Fig. 13. As the irradiance level increases, the Nyquist curves undergo a significant shift from the top right to the bottom left, indicating a decrease in the impedance of the PV panel.

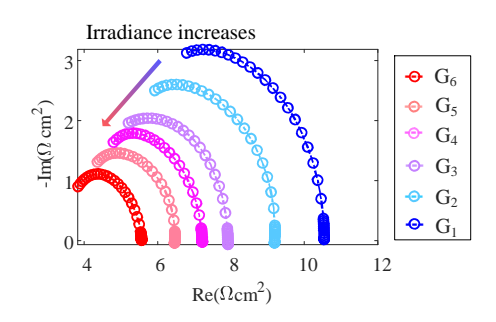


Figure 13: Experimental impedance spectra under different irradiance levels.

5.3. Verification under different partial shading conditions

Partial shading is a common condition during PV panel operation. At an irradiance level of G_6 , varying percentages of the same column of the PV panel are shaded using a shading board to simulate different levels of partial shading. The specific shading information is shown in Fig. 14 (a). Using the proposed method, the IS information of

the PV panel under these partial shading conditions was measured, and the experimental results are presented in Fig. 14 (b).

As the partial shading percentage increases, the Nyquist curve shifts from bottom left to top right, resembling the behavior observed under decreasing irradiance levels. When the partial shading percentage reaches the threshold for bypass diode activation, the entire string of PV cells operate under short-circuit conditions. This causes a sudden decrease in the impedance of the PV panel, as indicated by the blue line in Fig. 14 (b).

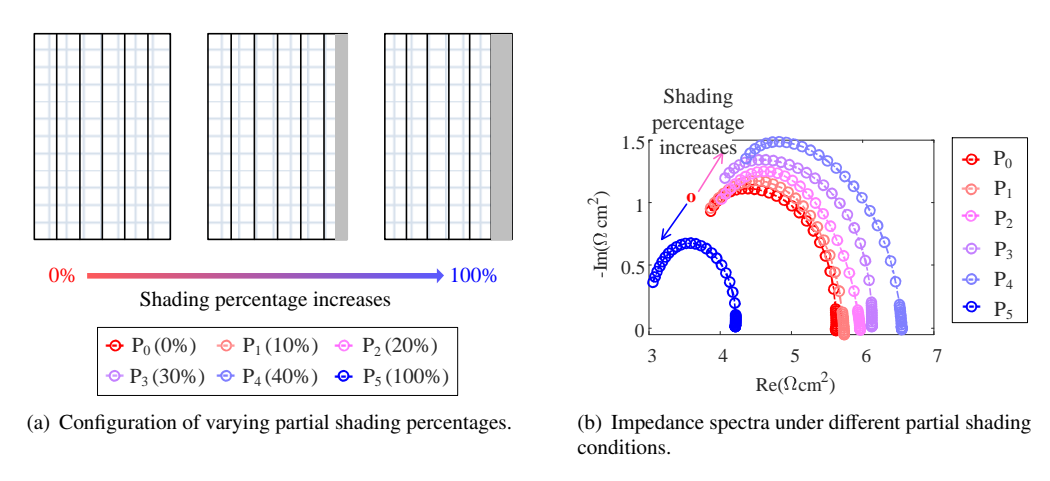


Figure 14: Experimental impedance spectra under different partial shading conditions.

Experiments conducted under varying irradiance levels and partial shading conditions validate the effectiveness of the proposed method for calculating the amplitude of the ac duty cycle in open-loop control for IS implementation. The method can acquire a set of reliable IS spectra, accurately reflecting the impedance characteristics of the PV panel.

6. Conclusion

Converter-based IS offers a practical solution for online characterization of a system without the need for additional equipment. It allows the injection of perturbation signals by directly adjusting the duty cycles of the connected converter. However, as analyzed in this study, there are two key challenges: the intrinsic resonant behavior of the converter during wide-band perturbation signal injection and the maximum perturbation signal frequency. Resonance may bring the operating points outside the quasi-linear operating region, while the maximum perturbation signal frequency limits the frequency range of the perturbation signal. Both aspects can impact the validity and accuracy of IS measurements. This work provides a detailed analysis on the influences of various parameters on the resonance and the maximum perturbation signal frequency, based on the small-signal transfer function of a conventional boost converter. These parameters include parasitic resistances r_{pv} , r_{C1} , r_L , r_{on} , r_d and r_{dc} , converter components C_1 , L and C_{dc} , and operating parameters including the output voltage and current of the PV panel V_{pv} and I_{pv} , load resistance R_L and duty cycle D.

To ensure a sufficient and stable perturbation signal, an adaptive open-loop control method is proposed, which can suppress the influence of resonance by employing a variable amplitude of the ac duty cycle. The calculation method for determining the amplitude of the ac duty cycle is detailed. Experimental results verify that the proposed method injects perturbation signals with appropriate amplitudes, enabling the acquisition of effective IS spectra that can reflect changes in operating conditions. Compared with conventional workstation-based approaches, this method eliminates the need for expensive workstations and power amplifiers. It only requires updating the existing control algorithm and replacing a high-precision current sensor, without major modifications to the original hardware. This not only reduces cost but also enhances implementation flexibility, providing a feasible and extensible solution for other converter topologies and real-time monitoring of large-scale PV systems. Further work will focus on utilizing these IS measurements for online health monitoring and fault diagnosis of PV panels.

Acknowledgment

This work was supported by French national agency (ANR) project JCJC EREMITE (contract ANR-19-CE05-0008-01) and Chinese Scholarship Council (CSC), the EIPHI Graduate School (contract ANR-17-EURE-0002) and the Region Bourgogne Franche-Comté (Corresponding author: Zhixue Zheng).

References

- [1] M. Wang, J. Zhou, J. Ji, J. Song, and W. Ji, "Performance assessment of solar-driven electrolytic hydrogen production systems enhanced by cdte pv and sun-tracking device," *Applied Energy*, vol. 390, p. 125852, 2025.
- [2] J. Zuo, N. Y. Steiner, Z. Li, C. Cadet, and B. Christophe, "Optimal post-prognostics decision making for multistack fuel cells in transportation: toward joint load allocation and maintenance scheduling," *IEEE Transactions* on *Transportation Electrification*, vol. PP, p. 1, 2024.
- [3] W. Tang, Y. Huang, T. Qian, C. Wei, and J. Wu, "Coordinated central-local control strategy for voltage management in pv-integrated distribution networks considering energy storage degradation," *Applied Energy*, vol. 389, p. 125684, 2025.
- [4] N. Kumar, "EV Charging Adapter to Operate With Isolated Pillar Top Solar Panels in Remote Locations," *IEEE Transactions on Energy Conversion*, vol. 39, no. 1, pp. 29–36, 2024.
- [5] B. Talihati, S. Fu, B. Zhang, Y. Zhao, Y. Wang, and Y. Sun, "Community shared es-pv system for managing electric vehicle loads via multi-agent reinforcement learning," *Applied Energy*, vol. 380, p. 125039, 2025.
- [6] A. Bahadori and C. Nwaoha, "A review on solar energy utilisation in Australia," *Renewable and Sustainable Energy Reviews*, vol. 18, pp. 1–5, 2013.
- [7] X. Du, J. Meng, Y. Amirat, F. Gao, and M. Benbouzid, "Voltage Hysteresis Cancellation for Fast Impedance Measurements of Lithium-ion Batteries in Short Relaxation Process," *IEEE Transactions on Transportation Electrification*, vol. PP, p. 1, 2024.
- [8] Z. Ning, P. Venugopal, T. B. Soeiro, and G. Rietveld, "Computation-light AI models for Robust Battery Capacity Estimation based on Electrochemical Impedance Spectroscopy," *IEEE Transactions on Transportation Electrification*, vol. PP, p. 1, 2024.
- [9] S. M. Islam and S. Y. Park, "Precise Online Electrochemical Impedance Spectroscopy Strategies for Li-Ion Batteries," *IEEE Transactions on Industry Applications*, vol. 56, no. 2, pp. 1661–1669, 2020.
- [10] P. Jiang, J. Chen, L. Jin, and L. Kumar, "Adaptive Condition Monitoring for Fuel Cells Based on Fast EIS and Two-Frequency Impedance Measurements," *IEEE Transactions on Industrial Electronics*, vol. 70, no. 8, pp. 8517–8525, 2023.
- [11] X. Wang, Z. Zheng, M. Aillerie, J.-P. Sawicki, A. De Bernardinis, M.-C. Péra, and D. Hissel, "Control Strategies of Converter-Based Online Impedance Spectroscopy for Photovoltaic Panels," *IEEE Transactions on Industry Applications*, pp. 1–15, 2024.
- [12] Q. Zhang, C. G. Huang, H. Li, G. Feng, and W. Peng, "Electrochemical Impedance Spectroscopy Based State-of-Health Estimation for Lithium-Ion Battery Considering Temperature and State-of-Charge Effect," *IEEE Transactions on Transportation Electrification*, vol. 8, no. 4, pp. 4633–4645, 2022.
- [13] A. Geng, H. Hu, Z. Zhao, J. Chen, Y. Ge, K. Wang, and Z. He, "Short Binary Sequence-Based Fast Electrochemical Impedance Spectroscopy Measurement for Lithium-Ion Batteries," *IEEE Transactions on Transportation Electrification*, vol. PP, p. 1, 2024.

- [14] H. Yuan, R. Du, X. Wang, X. Wei, and H. Dai, "Advanced Online Broadband Impedance Spectrum Acquisition of Fuel Cells by S-Transform," *IEEE Transactions on Industrial Electronics*, vol. 70, no. 4, pp. 3740–3750, 2023.
- [15] D. Xiang, C. Yang, H. Li, Y. Zhou, S. Zhu, and Y. Li, "Online Monitoring of Lithium-Ion Battery Internal Temperature Using PWM Switching Oscillations," *IEEE Transactions on Power Electronics*, vol. 38, no. 1, pp. 1166–1177, 2023.
- [16] J. A. Qahouq and Z. Xia, "Single-Perturbation-Cycle Online Battery Impedance Spectrum Measurement Method with Closed-Loop Control of Power Converter," *IEEE Transactions on Industrial Electronics*, vol. 64, no. 9, pp. 7019–7029, 2017.
- [17] E. Sadeghi, M. H. Zand, M. Hamzeh, M. Saif, and S. M. M. Alavi, "Controllable Electrochemical Impedance Spectroscopy: From Circuit Design to Control and Data Analysis," *IEEE Transactions on Power Electronics*, vol. 35, no. 9, pp. 9935–9944, 2020.
- [18] Z. Chen, Y. Zhang, C. Liu, R. Yang, and G. Chen, "A Novel Multi-sinusoidal PWM Excitation for Online Battery Impedance Spectroscopy Identification and Implementation by Reconfigurable Battery Systems," *IEEE Transactions on Transportation Electrification*, vol. PP, p. 1, 2024.
- [19] K. Zhang, R. Xiong, S. Qu, B. Zhang, and W. Shen, "Electrochemical Impedance Spectroscopy: A Novel High-Power Measurement Technique for Onboard Batteries Using Full-Bridge Conversion," *IEEE Transactions on Transportation Electrification*, pp. 1–11, 2024.
- [20] T. N. Gücin and L. Ovacik, "Online Impedance Measurement of Batteries Using the Cross-Correlation Technique," *IEEE Transactions on Power Electronics*, vol. 35, no. 4, pp. 4365–4375, 2020.
- [21] X. Wang, X. Wei, Q. Chen, and H. Dai, "A Novel System for Measuring Alternating Current Impedance Spectra of Series-Connected Lithium-Ion Batteries with a High-Power Dual Active Bridge Converter and Distributed Sampling Units," *IEEE Transactions on Industrial Electronics*, vol. 68, no. 8, pp. 7380–7390, 2021.
- [22] Q. Li, H. Wang, T. Wang, X. Li, Y. Liu, W. Chen, and Z. You, "Online Diagnosis Method of Water Management Faults Based on Hybrid-Frequency Electrochemical Impedance Spectroscopy for PEMFC," *IEEE Transactions on Transportation Electrification*, pp. 1–10, 2024.
- [23] J. Shen, H. Homayouni, and J. Wang, "Converter-Based Electrochemical Impedance Spectroscopy for High-Power Fuel Cell Stacks with Resonant Controllers," *IEEE Transactions on Industrial Electronics*, vol. 68, no. 9, pp. 8819–8828, 2021.
- [24] L. Shelembe and P. Barendse, "An Adaptive Amplitude-Modulated Pseudo-Random Binary Sequence Excitation for Converter-Based Impedance Spectroscopy Characterization of Photovoltaic Modules," *IEEE Transactions on Industry Applications*, vol. 59, no. 2, pp. 2007–2018, 2023.
- [25] X. Wang, Z. Zheng, M. Aillerie, M.-C. Pera, and D. Hissel, "Online health monitoring of silicon pv panels by converter-based impedance spectroscopy: Panel-level equivalent circuit model and health feature extraction," *IEEE Transactions on Industrial Electronics*, pp. 1–9, 2025.
- [26] H. H. Abbasali and S. Jafarabadi Ashtiani, "Online Broadband Battery Impedance Spectroscopy Using Current-Mode Boost Converter," *IEEE Transactions on Instrumentation and Measurement*, vol. 71, pp. 1–8, 2022.
- [27] X. Wang, Z. Zheng, M. Aillerie, A. De Bernardinis, M.-C. Péra, and D. Hissel, "Online Impedance Spectroscopy Characterization of PV Panels by Studying Resonant Behavior of Boost Converter," in 2023 IEEE Transportation Electrification Conference & Expo (ITEC), pp. 1–7, 2023.
- [28] E. Romero-Cadaval, G. Spagnuolo, L. G. Franquelo, C. A. Ramos-Paja, T. Suntio, and W. M. Xiao, "Grid-connected photovoltaic generation plants: Components and operation," *IEEE Industrial Electronics Magazine*, vol. 7, no. 3, pp. 6–20, 2013.

- [29] X. Yuan, J. C. Sun, M. Blanco, H. Wang, J. Zhang, and D. P. Wilkinson, "AC impedance diagnosis of a 500 W PEM fuel cell stack. Part I: Stack impedance," *Journal of Power Sources*, vol. 161, no. 2, pp. 920–928, 2006.
- [30] E. R. da Silva and M. E. Elbuluk, Fundamentals of Power Electronics, vol. 59. 2013.
- [31] J. Giner-Sanz, E. Ortega, and V. Pérez-Herranz, "Total harmonic distortion based method for linearity assessment in electrochemical systems in the context of eis," *Electrochimica Acta*, vol. 186, pp. 598–612, 2015.

Appendix

The parameters of the PV panel

Name	Symbol	Value
Power class	P_{mpp}	310 W
	Temperature Coefficients	-0.4%/°C
Maximum power voltage	$V_{ m mpp}$	32.3 V
Maximum power current	$I_{ m mpp}$	9.56 A
Open-circuit voltage	$V_{ m oc}$	39.6 V
	Temperature Coefficients	-0.3%/°C
Short-circuit current	$I_{\rm sc}$	9.95 A
	Temperature Coefficients	+0.04%/°C
Standardized test temperature	T	25 °C
Standardized test irradiance	G	1000 W/m ²

Table 1: Photovoltaic Module Parameters (RECOM-Sillia 60M310)

Calculation of the transfer function

The detailed switching states are illustrated in Fig. 1 below: when the switch T is on, the circuit state is shown in Fig. 1(a); when the switch T is off, the circuit state is depicted in Fig. 1(b).

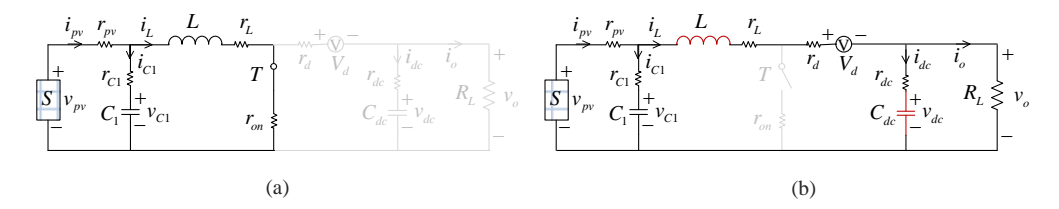


Figure 1: State circuits of the boost converter: (a) when the switch T is on, (b) when the switch T is off.

Substituting the variables after the small-signal perturbation into Equations (1) and (2) in the main text, and applying the Laplace transform, the small-signal expressions of all state variables can be written as:

$$\begin{cases} \hat{v}_{o}(s) = \frac{1}{(sC_{dc} + \frac{1}{R_{L}} + \frac{sC_{dc}r_{dc}}{R_{L}})} \cdot (\hat{i}_{L}(s)(1 - D)(sC_{dc}r_{dc} + 1) - \hat{d}(s)I_{L}(sC_{dc}r_{dc} + 1)) \\ \hat{v}_{PV}(s) = sL\hat{i}_{L}(s) + \hat{i}_{PV}(s)r_{PV} + \hat{i}_{L}(s)(r_{L} + r_{d}) + D\hat{i}_{L}(s)(r_{on} - r_{d}) + \hat{d}(s)I_{L}(r_{on} - r_{d}) \\ - \hat{d}(s)V_{d} + (1 - D)\hat{v}_{o}(s) - \hat{d}(s)V_{o} \end{cases}$$

$$(1)$$

$$\hat{i}_{PV}(s) = \frac{1}{(1 + sC_{1}r_{PV} + sC_{1}r_{C1})} \cdot (sC_{1}\hat{v}_{PV}(s) + \hat{i}_{L}(s)(1 + sC_{1}r_{C1}))$$

Then the small-signal transfer function from the duty cycle to the output current of the PV panel, i.e., $G_{i_{pv}-d}(s)$ indicated in Equation (4) in the main text can be derived.

Meanwhile, the transfer function in zero/pole form is adapted:

$$G_{i_{PV}-d}(s) = \frac{K_{i_{L}-d0} \,\omega_{0-i_{PV}} \,Q \,\omega_{0-i_{L}}^{2}}{\omega_{z-i_{PV}} \,\omega_{z-i_{L}}} \frac{(s+\omega_{z-i_{PV}})(s+\omega_{z-i_{L}})}{(s+\omega_{0-i_{PV}}) \left(s+\frac{\omega_{0-i_{L}}}{2Q}+\omega_{0-i_{L}} \,\sqrt{\frac{1}{4Q^{2}}-1} \,i\right) \left(s+\frac{\omega_{0-i_{L}}}{2Q}-\omega_{0-i_{L}} \,\sqrt{\frac{1}{4Q^{2}}-1} \,i\right)}$$
(2)

Corresponding zeros and poles:

• Zeros:
$$-\omega_{z-i_{PV}}$$
 and $-\omega_{z-i_L}$

• Poles:
$$-\omega_{0-i_{PV}}$$
, $-\frac{\omega_{0-i_L}}{2Q} - \omega_{0-i_L} \sqrt{\frac{1}{4Q^2} - 1} i$ and $-\frac{\omega_{0-i_L}}{2Q} + \omega_{0-i_L} \sqrt{\frac{1}{4Q^2} - 1} i$